Please cite this paper as

Li J and Zhu S (2021) Tunable Electromagnetic Damper with Synthetic Impedance and Self-powered Functions. Mechanical Systems and Signal Processing. 159: 107822. https://doi.org/10.1016/j.ymssp.2021.107822

Tunable Electromagnetic Damper with Synthetic Impedance and Self-powered Functions

Jin-Yang LI and Songye ZHU*

Department of Civil and Environmental Engineering, The Hong Kong Polytechnic University, Kowloon, Hong Kong, China

*Corresponding author: Prof. S. Zhu, Email: ceszhu@polyu.edu.hk

---

ABSTRACT:

Electromagnetic dampers (EMDs), which are regarded as an emerging type of dampers, have recently drawn increasing research interests in structural vibration control due to their unique advantages over conventional damper types. Although advanced synthetic impedance and energy harvesting functions of EMDs have been separately investigated, their integration has not been explored to the best of the authors' knowledge. The major obstacle herein is that the former versatile damper behavior is normally realized by consuming input energy, whereas the latter can only provide pure damping behavior comparable to passive viscous dampers while producing output energy. To fill this research gap, this study proposes a novel H-bridge circuit based EMD (HB-EMD), which allows bidirectional power flow between the EMD and the energy pool, and enables the realization of versatile damper behavior with the salient self-powered feature. The system design, working mechanism, synthetic impedance technique, power analyses, and emulation of various conventional dampers by using HB-EMD, are analytically, numerically, and experimentally examined. Scalability issues of HB-EMD are also discussed to shed light on future large-scale applications.

1. Introductions

A great variety of dampers, including passive, semi-active, and active types, have been widely adopted in the vibration control of mechanical and civil structures [1, 2]. Among these dampers, electromagnetic damper (EMD) is an emerging type that has drawn growing attention given its unique ability of providing energy transformation and exchange between mechanical and electrical systems. In comparison with the conventional dampers, EMDs possess some representative advantages as follows:

1. Owing to the analogue relations between mechanical and electrical systems [3], as show in Eq. (1), conventional mechanical elements or dampers can be emulated by EMDs by adopting the corresponding electrical elements:

$$m = K_{\text{em}}^2 C, \quad c = K_{\text{em}}^2 / R, \quad k = K_{\text{em}}^2 / L, \tag{1}$$

where C, R, and L stand for the capacitance, resistance, and inductance in an electrical circuit, respectively; m, c, and k stand for the inertance, damping, and stiffness coefficients in a mechanical system, respectively; and K_{em} is known as the motor constant of EMD.

2. The electric elements are generally compact in size and maintenance friendly [4]. Hence, the complex damper behavior, which can barely be achieved mechanically, is enabled by integrating various electrical elements or subcircuits into a single circuit board.

3. From an energy perspective, the kinetic energy embodied in excessive vibrations of mechanical structures can be transformed into electrical energy by EMDs, which can be potentially harvested [5-8]. By contrast, conventional dampers normally dissipate structural kinetic energy directly into ambient heat.

4. EMDs, as solid-state dampers, prevent oil leakage problem commonly seen in some conventional dampers (e.g., viscous fluid damper [VFD] and magnetorheological damper) [9].

5. Overheat problem due to energy dissipation may degrade damper behavior, provided that the fluid viscosity is typically temperature sensitive. Moreover, the accumulated heat in the fluid may accelerate the aging of sealing rubber rings and consequently undermine the damper life cycle. By contrast, EMDs can transform structural kinetic energy into electrical energy that can be either stored or shunted away. Consequently, the side effects due to damper local overheat problems are eradicated.

In view of the above-mentioned advantages, substantial research has been carried out on either vibration control or energy harvesting by using EMDs. Yan et al. [10] casted a review on vibration control techniques by using EMDs and piezoelectric (PZT) transducers. The passive control of a single degree of freedom (SDOF) structure by using an EMD was studied, wherein the EMD behavior was controlled by the external impedance [11, 12]. Vibration control of a forced-vibrating SDOF system coupled with EMD was well discussed by Inoue et al. [13]. Zhu et al. **[**14**]** examined an electromagnetic inertial mass device with an energy harvesting potential. Ning et al. [15] adopted an electromagnetic device to realize a variable

seat suspension. Yan et al. [16] adopted EMD to apply nonlinear damping to a permanent magnetic based bistable isolator. Li et al. [17] proposed a failure-free EMD shock absorber with energy harvesting potential. Zhang and Wang [18] conducted parameter study and optimization on a half-vehicle suspension incorporating EMD. Moreover, the auxiliary resistance of the electrical elements (e.g., resistor, inductor) used in the EMDs will deteriorate the control performances of EMDs [19, 20]. Accordingly, Li and Zhu [3] proposed the use of a negative impedance converter with voltage inversion (VNIC) to solve this bottleneck at the cost of additional energy input. Zhu et al. [21, 22] adopted EMDs to harvest energy and provide control behavior comparable to a viscous damper.

On the one hand, the existing literature revealed that the versatile behavior of EMDs enabled by the use of shunt circuits or synthetic impedance technique can achieve superior adaptive performance in the structural vibration control. On the other hand, dual-function EMDs have been developed to simultaneously provide energy harvesting and modest vibration control performance, wherein the damper behavior is only comparable to typical viscous dampers. Therefore, a natural question herein will be whether we can establish a novel dual-function EMD that can provide versatile damper behavior via synthetic impedance while harvesting energy simultaneously. To the best of our knowledge, the integration of these two advanced characteristics of EMDs is still absent in the existing literature.

Inspired by the attractive feature of the H-bridge circuit that grants bidirectional power flow between the EMD and the energy pool [7], an H-bridge circuit-based EMD (HB-EMD) is proposed in this study to fill the research gap. Conventionally, H-bridge circuits are often known as typical switch-mode rectifiers [23] that are widely adopted in motor control or converters between AC and/or DC. Recently, a growing interest is paid to their applications in energy harvesting [7, 24]. Bowden et al. [25, 26] used a modified H-bridge circuit to tune the electromagnetic (EM) energy harvester to enhance the energy harvesting efficiency. Liu et al. [27] adopted an H-bridge circuit to improve the energy harvesting efficiency of PZT materials. Hsieh et al. [23] utilized a similar H-bridge topology in an energy regenerative suspension system by emulating various resistances and realized semi-active skyhook control.

Hence, this study will investigate the proposed HB-EMD with synthetic impedance and energy harvesting functions, laying foci on the system topology, working mechanism, power balance, and realization of synthetic impedance (i.e., equivalent versatile damper behavior). Subsequently, an HB-EMD prototype is manufactured and experimentally tested to validate its feasibility and effectiveness. Finally, the scalability issue of the proposed HB-EMD is discussed to examine the availability of relevant elements compatible to large-scale applications.

2. HB-EMD

An HB-EMD is proposed in this study to synthesize various electrical impedances to emulate versatile mechanical behavior according to Eq. (1). In particular, the system configuration, working principles, and power analyses of HB-EMD will be elaborated in this section.

2.1 System Configuration

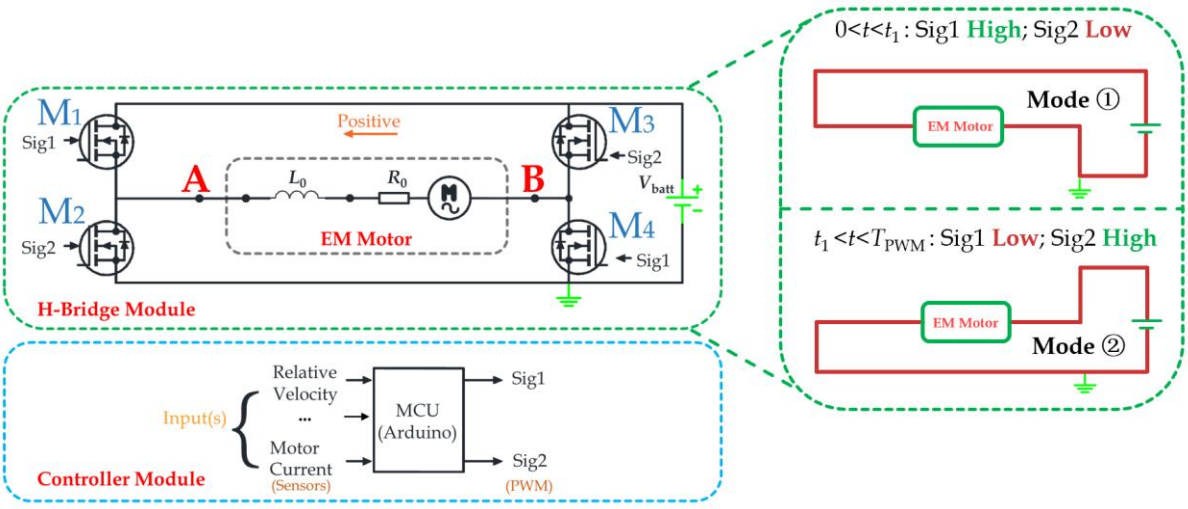

(a)

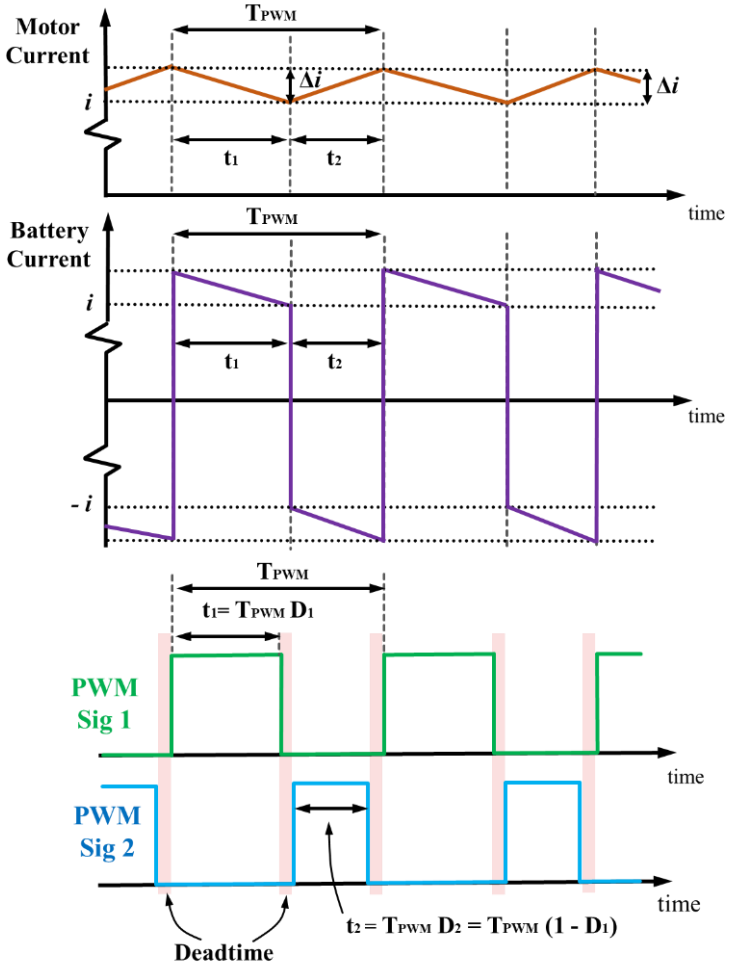

(b)

Fig. 1 System configuration of HB-EMD: (a) schematic of the system topology; (b) motor and battery currents under the corresponding PWM control signals (deadtime not in scale and for illustration purpose only)

Fig. 1(a) provides the topology of the proposed HB-EMD system, which mainly consists of three modules, namely, (a) electromagnetic motor module, (b) H-bridge module, and (c) controller module.

In Fig. 1(a), the EM motor module essentially models an EM motor by using an ideal electromotive force (*emf*) source in series connection with inner resistance (R_0) and inner inductance (L_0) due to the inherent material properties of the motor coils. The EM motor shall function as both a generator and an actuator. When the EM motor experiences a motion, an *emf* (i.e., voltage) will be generated at its coil ends; and when the current flows through the motor coil, a corresponding EM force will be generated:

$$V_{\mathrm{m}} = K_{\mathrm{em}} \cdot \dot{u}, \;\; f_{\mathrm{ctrl}} = -K_{\mathrm{em}} \cdot i \,, \tag{2}$$

where K_{em} is known as the motor constant determined by the physical properties of the EM transducer (such as magnetic flux density, coil size, and number of windings), V_{m} stands for the *emf* generated at the coil ends when a relative velocity ($\dot{u}$) is experienced between the two nodes of the EM transducer; and f_{ctrl} is the EM control force generated when a current (i) flows through the motor coil. A non-commutated DC linear motor is adopted in the experimental validation test in this study. Commutated brushless motor types that do not satisfy Eq. (2) are suitable for such applications.

The H-bridge module comprises four metal–oxide–semiconductor field-effect transistors (MOSFETs) arranged in an "H" shape and a rechargeable battery set. Specifically, the H-bridge circuit functions as the interface between the EM motor and the rechargeable battery set. The MOSFETs are commonly categorized into two types, namely, N-type MOSFET (i.e., NMOS) and P-type MOSFET (i.e., PMOS). NMOS is turned "on" when the gate-source voltage (V_{GS}) is high; and it will be turned "off" once V_{GS} is low. PMOS behaves in the opposite, being turned "on" when V_{GS} is low and vice-versa. In this study, all four MOSFETs in the H-bridge are NMOSs (high — on; low — off), with diagonal MOSFET sets (i.e., $M_1 - M_4$ and $M_2 - M_3$) controlled by two pulse width modulation (PWM) signals — *Sig* 1 and *Sig* 2, respectively. The rechargeable battery serves as an energy pool catering for the power exchange by either storing the harvested power or supplying power for the actuation. Although supercapacitors are also frequently used in energy harvesting applications, rechargeable batteries are considered a better option with a more stable output voltage. Therefore, a Ni-MH rechargeable battery set is adopted in our setup.

The control module determines the behavior of HB-EMD by executing the pre-coded algorithms and outputting the corresponding PWM signals (i.e., *Sig* 1 and *Sig* 2) to the H-bridge module. This module consists of a microcontroller unit (MCU) and relevant sensors (e.g., accelerometer and displacement sensor). The measured analogue signals from various sensors will be received by the MCU and subsequently converted into digital signals through an onboard A/D converter. These digital signals will then participate in the determination of the PWM control signals by following the pre-coded control algorithm that is burnt to the MCU chip. The PWM signals will be finally outputted to the MOSFETs to generate the desired control force through the EM transducer. In particular, the adopted MCU in this study is an Arduino Uno, which is one of the widely recognized open-source MCUs on the market. The

relevant codes reflecting the control algorithms are uploaded to the MCU through a C language-based integrated development environment(IDE).

2.2 Working Principles

When the proposed HB-EMD operates, two diagonal MOSFET sets (i.e., either M_1 and M_4 or M_2 and M_3 in Fig. 1(a)) controlled by the PWM signals (Fig. 1(b)) will be turned "on" and "off" in a consecutive reverse manner. However, these sets will never be turned "on" at the same time (i.e., *Sig*s 1 and 2 are high); otherwise, they will cause short-circuit between the battery and the ground. Consequently, only two states will be experienced by the H-bridge circuit in normal operation: (a) when PWM *Sig* 1 is high, MOSFETs M_1 and M_4 in Fig. 1(a) will be turned "on"; and *Sig* 2 has to be low, resulting in "off" states of MOSFETs M_2 and M_3, (Mode ① shown in Fig. 1(a)); and (b) the signals are reversed: *Sig* 1 is low, and *Sig* 2 is high, leading to "on" states of M_3 and M_4 and "off" states of M_1 and M_2 (Mode ② in Fig. 1(a)). These two modes reverse the connection directions of the EM motor to the battery. Given the voltage fluctuations experienced by the high-side MOSFETs (i.e., M_1 and M_3) provoked by the EM transducer, a full-bridge driver is adopted to ensure normal operations of the H-bridge circuit. The switching frequencies (f_{pwm}) of the two PWM signals (i.e., *Sig*s 1 and 2) are typically beyond thousands of Hertz. Accordingly, the PWM period is $T_{\text{PWM}} = 1/f_{\text{PWM}}$. Given that *Sig*s 1 and 2 are inverse from each other, if the duty cycle of *Sig* 1 is denoted as D_1, then that of *Sig* 2 will approximately be $D_2 = 1 - D_1$, where the duty cycle is defined as the fraction of "on" state duration (t_{on}) of a signal over the PWM period (i.e., $D = t_{\text{on}} / T_{\text{PWM}}$). In addition, a deadtime (t_{dt}) is further introduced to the control signals to prevent the aforementioned short-circuit phenomenon, which stands for an extreme short duration in the flip-over process between *Sig*s 1 and 2 when both of the signals are low, as shown in Fig. 1(b). Given that the duration of deadtime is nearly negligible compared with T_{PWM} (i.e., t_{dt} is only 1% of T_{PWM} or less), the relation $D_1 + D_2 \approx 1$ remains valid.

In our system topology shown in Fig. 1(a), the positive values are assigned to the current flowing through the EM transducer to the left and the *emf* across the EM transducer when the left-hand side voltage is higher. Within one period (T_{PWM}), M_1 and M_4 are "on" (i.e., M_2 and M_3 are automatically "off") during $t_1 = T_{\text{PWM}} \cdot D_1$ (i.e., *Sig* 1 is high, and *Sig* 2 is low); and the states reverse (M_1 and M_4 are "off", and M_2 and M_3 are "on") for the remaining time $t_2 = T_{\text{PWM}} D_2 = T_{\text{PWM}} \cdot (1 - D_1)$. Hence, according to Kirchhoff's voltage law (KVL), we have

$$V_{\text{m}} - V_{\text{batt}} - iR_{\text{t}} - L_0 \frac{\Delta i_1}{t_1} = 0, \qquad \text{when } 0 < t < t_1, \tag{3}$$

$$V_{\text{m}} + V_{\text{batt}} - iR_{\text{t}} - L_0 \frac{\Delta i_2}{t_2} = 0, \qquad \text{when } t_1 < t < T_{\text{PWM}}, \tag{4}$$

where V_{m} is the instant *emf* of the EM transducer; V_{batt} is battery voltage; R_{t} is the inherent circuit resistance accounting for both motor inner resistance (R_0) and other auxiliary resistances

from the connecting wires, MOSFETs (R_{MOS}), battery inner resistance, and so on; L_0 is the motor inner inductance; i is the circuit current; Δi_1 and Δi_2 are the fluctuations of current i during t_1 and t_2, respectively. The PWM frequency is generally several orders higher than the vibration frequency, and the EM transducer voltage (V_m) and battery voltage (V_{batt}) can be treated as constants within one PWM period.

Fig. 1(a) shows the current directions in two modes when the *emf* and motor current are both positive. Within one PWM period, the battery current reverses its direction (charge and discharge), whereas the motor current does not. The motor current change should be zero within one complete PWM period (i.e., $\Delta i_1 + \Delta i_2 = 0$, as shown in Fig. 1(b)), which will otherwise result in energy accumulation within L_0. Therefore, Eq. (5) can be obtained by solving Eqs. (3) and (4) as follows:

$$i = \frac{V_m + V_{batt}(1-2D_1)}{R_t}. \tag{5}$$

Eq. (5) essentially reveals that the EM motor current in HB-EMD is solely proportional to the input PWM duty cycle (D_1) given the nearly constant V_m and V_{batt} values in a PWM cycle.

Further substituting Eq. (5) into Eq. (2) delivers the EM control force (f_{ctrl}) as follows:

$$f_{ctrl} = -K_{em} \cdot \left[\frac{K_{em}\dot{u} + V_{batt}(1-2D_1)}{R_t} \right], \tag{6}$$

where $\dot{u}$ is the relative velocity between the two nodes of the EM transducer. Eq. (6) illustrates that a desired control force of HB-EMD can be obtained by inputting the corresponding PWM duty cycle (i.e., D_1) when the motor velocity ($\dot{u}$) is known.

For example, a theoretical function between the instant current and the corresponding duty cycle suggested by Eq. (5) is provided in a blue dashed line in Fig. 2. The results from Simulink simulation (black triangle) and experimental verification (red circle) are also provided in the figure. The corresponding Simulink model and the experimental setup will be elaborated in Subsections 2.4 and 3.1, respectively. The major parameters corresponding to Fig. 2 are measured as: inductance of L_0 = 0.1 H, inherent circuit resistance of R_t = 16 Ω, and a battery voltage of V_{batt} = 12 V. A constant motor *emf* is represented by a second battery with a measured voltage of V_m = 2.5 V. These parameters are selected in accordance with the experimental verifications in Subsection 3.1.

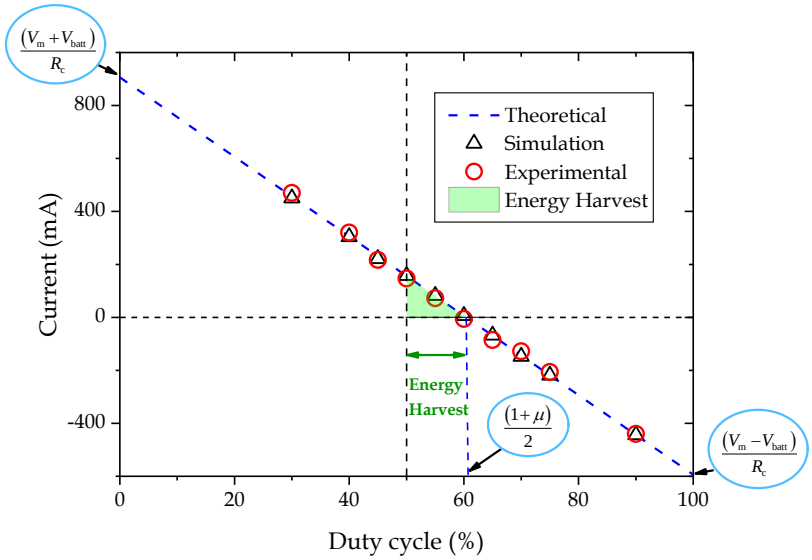

Fig. 2 Linear relation between the EM motor current and the PWM duty cycle (D_1) of Sig 1

Given range $D_1 \in [0,1]$, the achievable ranges for the motor current and the control force are constrained within

$$i \in \left[\frac{V_m - V_{batt}}{R_t}, \frac{V_m + V_{batt}}{R_t}\right],$$
$$f_{ctrl} \in \left[\frac{-K_{em}(V_m - V_{batt})}{R_t}, \frac{-K_{em}(V_m + V_{batt})}{R_t}\right]. \quad (7)$$

The corresponding upper and lower bounds of the motor current are also marked in Fig. 2.

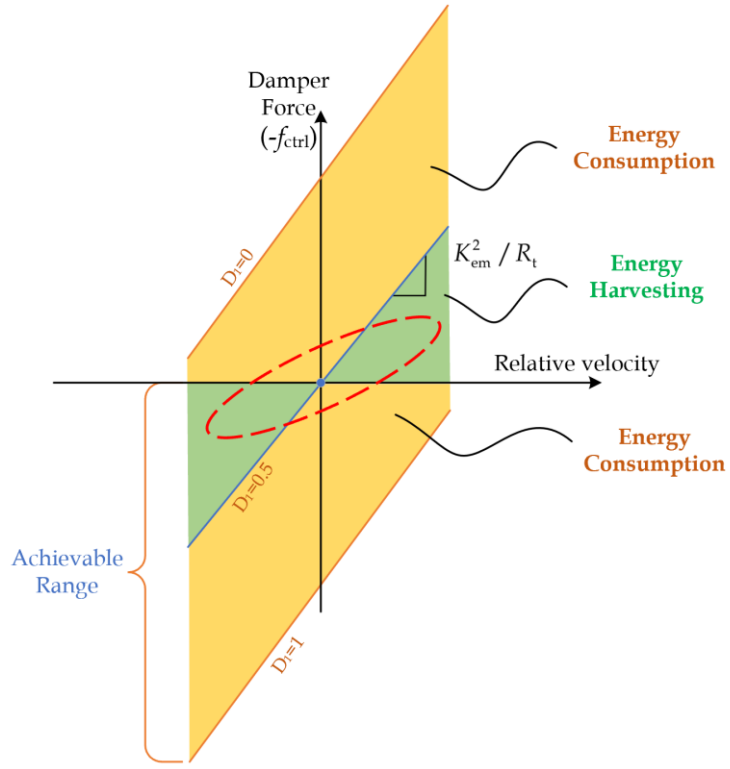

Fig. 3 Relation between the damper force and the relative velocity between the two nodes showing the ranges of power consumption and harvesting

The relation between the control force and the motor relative velocity suggested by Eq. (6) is shown in Fig. 3. The upper and lower bounds, which define the achievable range of the control force in Eq. (7), correspond to the cases when $D_1 = 0$ and 1, respectively. Any desired control force within the mentioned range can be generated by assigning the corresponding duty cycle (D_1) on the basis of Eq. (6). According to Eq. (7), the achievable control force range can be expanded by adopting a large power source voltage V_{batt}, a large machine constant K_{em}, and/or a small inherent resistance R_t.

Given that any damper force within the achievable range (Eq. (7)) can be generated, the key question is how to generate favorable mechanical behavior of the damper by manipulating the duty cycle of the H-bridge circuit in a responsive manner.

2.3 Realization of Synthetic Impedance

Eq. (1) implies that the versatile mechanical damper behavior can be emulated by employing the corresponding electrical elements in the shunt circuits [3], wherein the resistor, capacitor, and inductor can produce in-phase, phase-lead, and phase-lag currents (or equivalently the forces), respectively. Such a phase control can be achieved by a synthetic impedance technique without the actual use of the above-mentioned electric elements. Fleming et al. [28] proposed a synthetic impedance circuit compatible to a piezoelectric transducer consisting of three OPAMPs and one *dSPACE* digital signal processor (DSP). Necasek et al. [29] followed a

similar approach and further improved the work by replacing the DSP with an MCU (ARM Cortex-M4F). A synthetic impedance circuit prototype is subsequently manufactured by Necasek et al. [29] with feasibility numerically and experimentally validated.

In this study, a new synthetic impedance technique is developed, wherein the electric impedance is synthesized by directly regulating voltage — current relations using the H-bridge circuit following Eq. (5). Compared with the use of resistors, capacitors, and inductors [3], the new synthetic impedance technique enables more convenient tuning of the damper behavior, which is highly desirable in vibration control applications.

If the target electrical impedance to be synthesized is Z, then we will have the following relation in the *Laplace* domain (s domain):

$$\frac{I(s)}{U(s)} = \frac{1}{Z(s)}, \tag{8}$$

where I(s) and U(s) are the Laplace transform of i and V_m, respectively. The above continuous-time equation in the s domain can be transformed to a discrete-time one in the z domain on the basis of the Tustin method (bilinear transform):

$$\frac{I}{U} = \frac{k_1 + k_2(1/z) + k_3(1/z)^2}{k_4 + k_5(1/z) + k_6(1/z)^2}, \tag{9}$$

where k_1 to k_6 are the coefficients in the discrete function. Consequently, Eq. (9) can be rewritten as follows:

$$I_n = (k_1 U_n + k_2 U_{n-1} + k_3 U_{n-2} - k_5 I_{n-1} - k_6 I_{n-2}) / k_4, \tag{10}$$

where subscripts n, $n-1$, and $n-2$ denote the values of the present, previous-one, and previous-two frames (steps), respectively. Eq. (10) reveals that the desired current (i) of the present step can be calculated using merely the voltages and currents from the previous two steps.

Given a sampling interval of $t_s = 1/f_s$, where f_s is the sampling frequency of the MCU, this discretization can be carried out by using the Matlab command "c2d". For example, the coefficients in Eq. (10) for a sampling frequency of 200 Hz can be obtained to emulate an electrical impedance of $Z = R + 1/(Cs)$ representing a series connected resistance of R = 30 Ω and capacitance of $C = 5\times10^{-4}$ F. The results are listed in Table 1. According to Eq. (1), the resistance and capacitance in the example correspond to a damping coefficient of 56 Ns/m and an inertance coefficient of 0.84 kg connected in series.

Table 1. Parameters of the discretized transfer function of the example (R = 30 Ω and C = 5×10^{-4} F)

Parameters	Value
k_1	0.0286
k_2	−0.0286
k_3	0
k_4	1
k_5	−0.7143
k_6	0

Once the target current in the present frame is computed on the basis of Eq. (10), the desired control duty cycle can be determined by rewriting Eq. (5) as follows:

$$D_1 = \frac{1}{2} + \frac{V_m - iR_t}{2V_{batt}}. \tag{11}$$

where V_{batt} and R_t are constants; and V_m and i are the *emf* and current of the present step (i.e., U_n and I_n), respectively.

2.4 Numerical Model

To this end, the working mechanism of the proposed HB-EMD in the emulation of a mechanical damper has been thoroughly introduced. Fig. 4 provides the block diagram of an HB-EMD installed to a structure under external excitation. The model is consistent with the experimental setup described in Subsection 3.1. The topologies of the three major modules of HB-EMD (namely, the MCU, H-bridge circuit, and EM transducer) can be clearly identified in Fig. 4, where blocks J, G, and H correspond to Eqs. (10), (11), and (5), respectively.

Fig. 5 provides the corresponding Simulink model of the proposed HB-EMD that runs in a *powergui* environment with a fixed discretized time step of 10^{-6} s for the simulation. In particular, the logic circuit showing the derivation of the present-frame current by adopting the voltage and current from the previous two frames is shaded in green, where the corresponding parameters (i.e., k_1 to k_6) match those from Eqs. (9) and (10). The derivation herein is based on another discrete time step of 0.01 s (i.e., sampling time) that corresponds to the sensing frequency designed in the MCU.

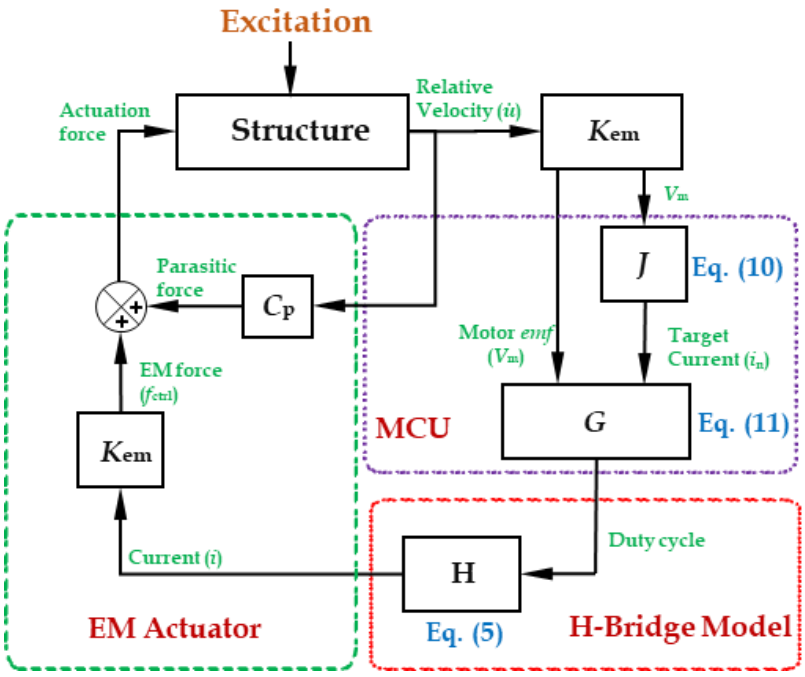

Fig. 4 Block diagram showing the realization of synthetic impedance with the proposed system

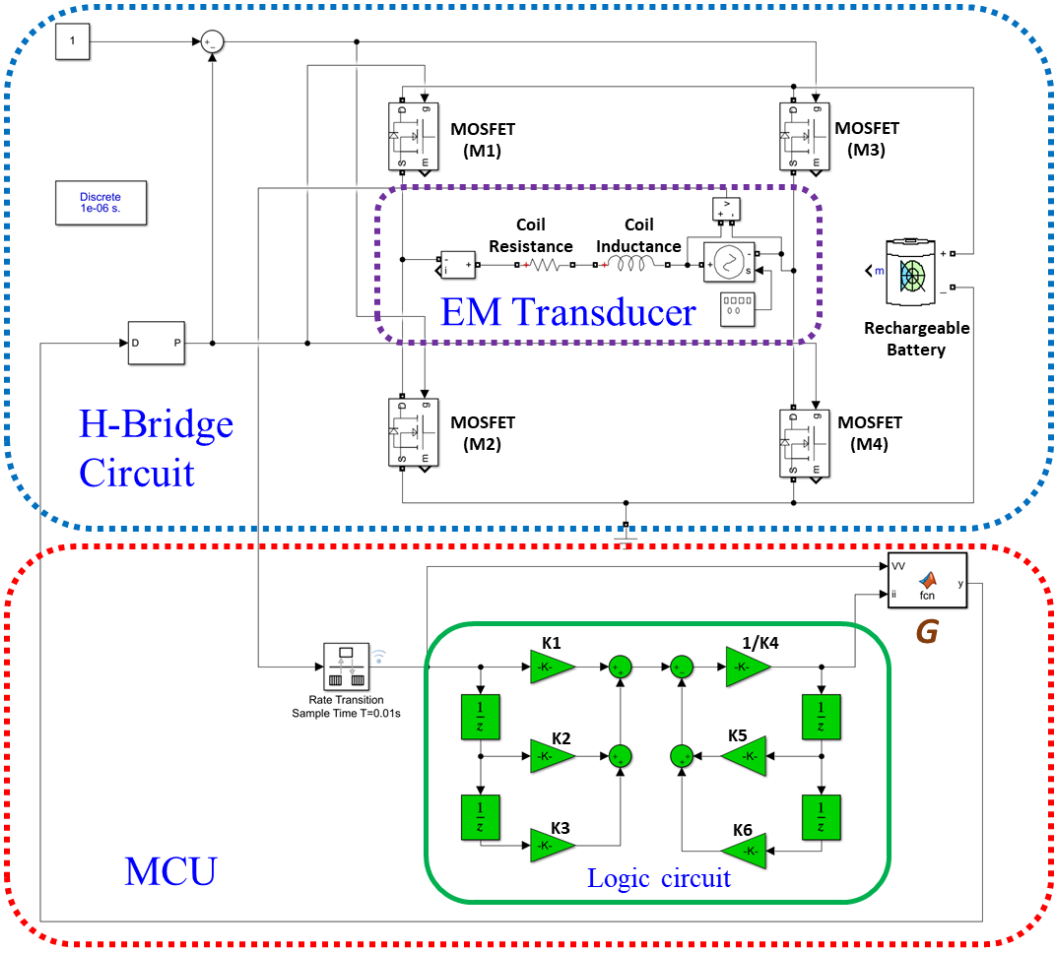

Fig. 5 SIMULINK model of HB-EMD with the realization of synthetic impedance

2.5 Power Analysis

The current (i) flowing through the EM transducer remains almost constant within one PWM cycle, as shown in Eq. (5); whereas the current through the battery maintains the same amplitude but flips between "in" and "out" (i.e., two directions) due to the switching of the H-bridge circuit, as shown in Fig. 1(b). If the current (i) in the EM transducer is positive (i.e., flowing from right to left), then the battery is charged and discharged during t_1 and t_2, respectively, as elaborated in Eqs. (3) and (4). Hence, the relative durations of t_1 and t_2 determines if HB-EMD harvests or consumes energy within one PWM cycle: harvesting energy when $t_1 > t_2$ and consuming energy when $t_1 < t_2$. Consequently, the instantaneous power (P_E) can be calculated as follows:

$$P_E = V_{batt} i (2D_1 - 1), \tag{12}$$

where the instantaneous power P_E is essentially the average output power in one PWM cycle. Substituting Eq. (5) into Eq. (12) yields

$$P_E = V_m i - i^2 R_t . \tag{13}$$

Eq. (13) can also be independently derived on the basis of the conservation of energy, given that the rate of work done by the EM transducer is $V_m i$, leaving the only power loss ($i^2 R_t$) due to the circuit resistance that is converted into ambient heat. According to Eqs. (12) and (13), the value of P_E is positive when the system is harvesting energy, whereas P_E is negative when the system is consuming energy from the battery.

Hence, the corresponding power harvesting condition for the current (i) flowing in the EM transducer can be obtained on the basis of Eq. (13) as follows:

$$V_m / i > R_t . \tag{14}$$

Consequently, the duty cycle for the positive output power ($P_E > 0$) can be obtained by combining Eqs. (5) and (12):

$$D_1 \in \begin{cases} \left[\frac{1}{2}, \frac{1+\mu}{2}\right] & \text{if } \mu > 0 \\ \left[\frac{1+\mu}{2}, \frac{1}{2}\right] & \text{if } \mu < 0 \end{cases}, \tag{15}$$

where voltage ratio $\mu = V_m / V_{batt}$, the battery voltage V_{batt} is always positive and nearly constant, and the *emf* V_m can be either positive or negative.

The green shaded area observed in Fig. 2 corresponds to such a power harvesting range when $\mu > 0$ (i.e., $V_m > 0$). If a sinusoidal input is assigned to HB-EMD (i.e., V_m is sinusoidal), then the energy harvesting and energy dissipation ranges in the time domain are depicted in Fig. 6, a combination of which provides the overall achievable range in agreement with Eq. (7). The critical energy harvesting line is determined as $i_{crit} = V_m / R_t$ when $D_1 = 0.5$ (i.e., the boundary dividing power harvesting and power consumption zones seen from Eq. (15)).

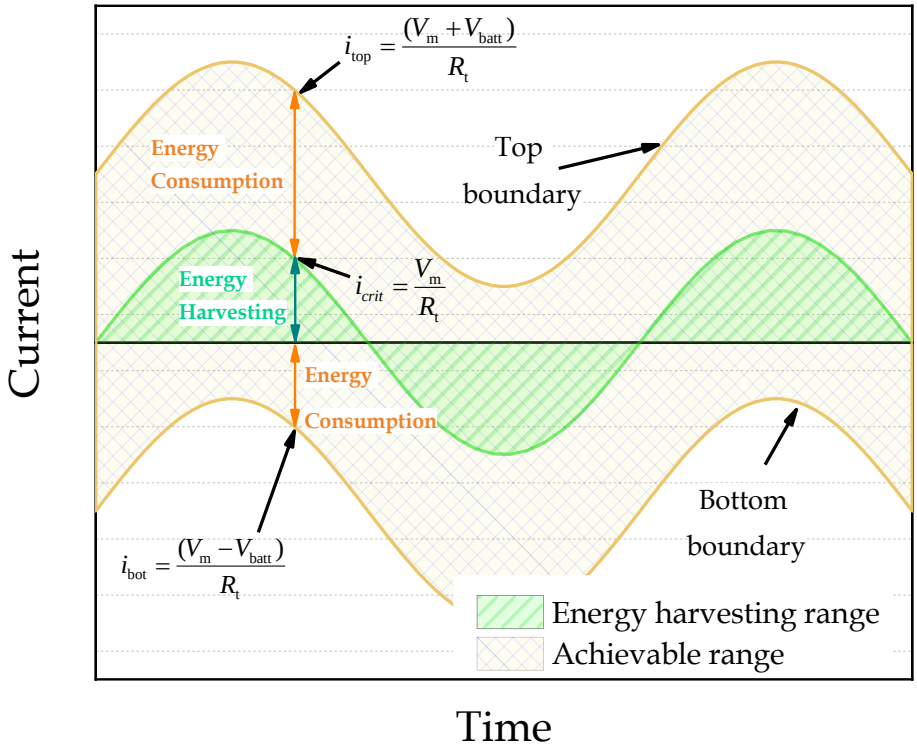

Fig. 6 Ranges for energy harvesting and consumption

Substituting Eqs. (2) and (5) into Eq. (12) and making it greater than zero leads to the following power-harvesting condition in the force–velocity relation:

$$0 < -f_{ctrl} / \dot{u} < K_{em}^2 / R_t \,. \tag{16}$$

The green shaded area in Fig. 3 shows the power harvesting zone in the actuator force–velocity plane, and the yellow area represents the power consuming zone. The green shaded area is only part of the first and third quadrants. The boundary is defined using a line with a slope of K_{em}^2 / R_t, which corresponds to the duty cycle $D_1 = 0.5$ and zero output power. Thus, a minimal R_t value can enlarge the power harvesting (i.e., green) zone in Fig. 3.

Although an overall energy harvesting scenario is desired, it is unnecessary to keep the force–velocity relation always in the power harvesting zone to achieve such a goal. Within a given time duration (0–t), the harvested or consumed energy can be calculated as follows:

$$E = \int_0^t V_{batt} i (2D_1 - 1) \cdot dt \,. \tag{17}$$

The dashed loop in Fig. 3 shows a representative control force–velocity relation in a vibration cycle. The HB-EMD can operate in an overall energy harvesting mode, provided that the force–velocity loop covers more green area than yellow area. The rechargeable battery stores the harvested power temporarily in the green zone and reuses this power in the yellow zone to generate the corresponding control forces.

The above-mentioned derivation assumes that the structural vibration frequency is considerably lower than the PWM switching frequency of the H-bridge circuit. The former typically ranges from several to hundreds of hertz, whereas the latter typically starts from

thousands of hertz or even higher. Otherwise, the control force will not be successfully achieved through the proposed setup.

Given an arbitrary synthetic impedance in the form of $Z = |Z| e^{j\alpha} = \Re(Z) + \Im(Z) \cdot j$, where $\alpha = \tan^{-1}[\Re(Z)/\Im(Z)]$ and $\Re(Z)$ and $\Im(Z)$ are the real and imaginary parts of *Z*, respectively, the average power flow under a sinusoidal input generating a motor *emf* of $V_{\mathrm{m}} = |V_{\mathrm{m}}| e^{\omega t}$ can be calculated using Eq. (17) over one period *T* of the sinusoidal input as follows:

$$\bar{P}_{\mathrm{E}} = \frac{1}{T}\int_0^T P_{\mathrm{E}} \cdot dt = \frac{1}{2}\frac{|V_{\mathrm{m}}|^2}{|Z|^2}\left[\Re(Z) - R_{\mathrm{t}}\right], \tag{18}$$

where the *emf* period *T* is equal to the period of structural vibration.

Solving Eq. (18) > 0 leads to the following condition for overall energy harvesting

$$\Re(Z) > R_{\mathrm{t}}\,. \tag{19}$$

In accordance with Eq. (19), only the relative magnitudes between the real part of the synthetic impedance [i.e., the synthetic resistance $\Re(Z)$] and the circuit inherent resistance (R_{t}) will determine whether the HB-EMD will harvest energy or not. If $\Re(Z) > R_{\mathrm{t}}$, then the system harvests energy; otherwise, the system requires external energy input from the battery to realize the entitled impedance.

Hence, the critical equivalent damping dividing energy boundary in the HB-EMD design is as follows:

$$c_{\mathrm{critical}} = K_{\mathrm{em}}^2 / R_{\mathrm{t}}\,, \tag{20}$$

in concordance with Eq. (16).

3. Experimental Study

3.1 Experimental Setup

Fig. 7(a) shows a photo of the mechanical section of the experimental setup on a shake table [part #: APS 420, $0.59\,\mathrm{m} \times 0.36\,\mathrm{m} \times 0.28\,\mathrm{m}$ (H × W × L)]. Two EM transducers (i.e., control and sensing EM transducers) are connected to the same plate that is hung by four springs to the outer-frame fixed to the shake table). The control EM transducer functions as the one in HB-EMD. The two EM transducers here are adopted because the equivalent *emf* of the control EM transducer cannot be directly measured when it is connected to an external circuit. If the back *emf* (i.e., the open-circuit voltage) of the sensing EM transducer is measured as $V_{\mathrm{m,S}}$, then the desired back *emf* of the control EM transducer can be subsequently calculated as $V_{\mathrm{m,C}} = -V_{\mathrm{m,S}} \cdot K_{\mathrm{em,C}} / K_{\mathrm{em,S}}$ because both EM transducers have one end connected to the plate

while the other end to the outer-frame. Given that the signal $V_{m,S}$ can be directly collected by the MCU, no signal conditioner is needed in this sensing method. As shown in Fig. 4, only the sensing of the *emf* (i.e., equivalent local relative velocity) will be required in the feedforward control of HB-EMD to emulate diverse mechanical behavior. No other sensing signals or feedback loops are involved in the control algorithm.

Fig. 7(b) shows a detailed schematic of the mechanical section with the mentioned two EM transducers highlighted — sensing EM transducer (part #: Baldor LMNM2-1F5-1F1) on top and control EM transducer (part #: VCM Tech Co.) at the bottom. Motor constants of the two EM transducers and other relevant parameters are provided in Table 2. Consequently, a sinusoidal input can be applied to the EM transducers through this setup with $V_{m,C}$ measurable. An extra inductor (part #: Hammond 195T5) is further introduced to the control EM transducer to increase the motor inductance that subsequently smooths the current curve.

Absolute accelerations and displacements of the vibration plate and the fixed frame are further measured using accelerometers (part #: B&K 4370) and laser displacement sensors (part #: KEYENCE, LK-503), respectively. Control force generated by the EM transducer is measured using an axial loadcell. The motor current (i) is measured by recording the voltage difference across a small-value sensing resistor (R_s = 1 Ω). These sensing signals are only used in the performance measurement instead of in the control algorithm.

Fig. 8(a) shows a photo of the electrical section of the HB-EMD on a breadboard consisting of the H-bridge circuit module, rechargeable battery set, and MCU (part #: Arduino Uno, ATmega328, clock speed 16 MHz, 14 Digital I/O pins, four analog input pins; the typical power consumption is 250 mW). Nodes A and B in Fig. 8 correspond to the two end nodes of the control EM transducer in Fig. 7(b). Four MOSFETs (part #: IRF840A) are used in the H-bridge circuit. A full-bridge driver (part #: HIP 4082) is adopted in the setup to drive the high-side MOSFETs (i.e., M_1 and M_3 in Fig. 1) to eliminate the impact due to the voltage fluctuation across the EM transducer. Depending on the working condition, the deadtime value can be adjusted by altering the R_1 value in Fig. 8 referring to the user manual of the bridge driver. R_1 (10 kΩ) connected between pin 5 and the ground introduces a 0.5 μs deadtime to prevent potential short-circuit. The rechargeable battery set is made up of NiMH rechargeable batteries (part #: Varta) connected in series, providing a nominal voltage of 12 V. Arduino Uno is adopted in this study to examine the feasibility of the prototype. MCU energy consumption could be significantly reduced by shifting to other low-power options, such as Arduino Pro mini. In extremely energy-sensitive applications, a tailor-made MCU board can be constructed by removing unnecessary elements to further minimize the power consumption of the MCU module.

The sampling frequency of the MCU in the current setup is 200 Hz, and its output PWM frequency is 2 kHz. Except for the battery current, the sensing signals are collected by a data acquisition system (part #: KYOWA, EDX-100A) at a sampling frequency of 1 kHz. The battery current alters its direction in the same frequency as the PWM signals; thus, it is measured by a separate data acquisition system (part #: TiePie HS5) at a sampling frequency of 100 kHz, which is 50 times that of the PWM switching frequency (i.e., 50 points sampled

within 1 PWM period). Consequently, the experimental duty cycle can be read from the measured battery current with a resolution of 2%.

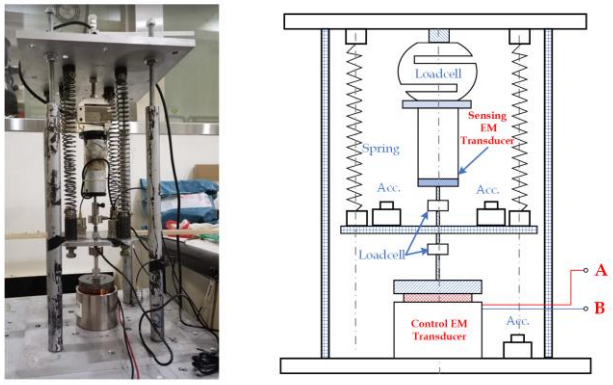

Fig. 7 Mechanical section of the experimental setup: (a) Photo; (b) Schematic drawing

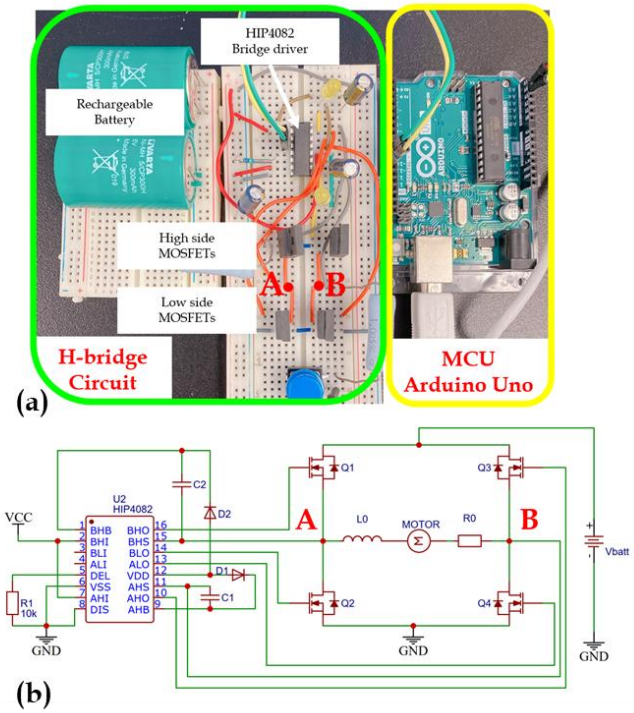

Fig. 8 Electrical section of the experimental setup: (a) in-situ photo; (b) schematic

Table 2. Major parameters of sensing and control EM transducers

Item	Parameters	Symbol	Value
Sensing EM transducer	Motor constant	$K_{em,S}$	7.474 Vs/m (or N/A)
Control EM transducer	Motor constant	$K_{em,C}$	41Vs/m (or N/A)
	Motor inner resistance	$R_{0,C}$	5.5 Ω
	Motor inductance	$L_{0,C}$	0.012 H

Circuit	Added inductance	$L_{0,added}$	0.1 H
	Sensing resistor	R_s	1 Ω
	Inherent resistance	R_t	16 Ω

3.2 Experimental Cases and Results

Four cases, denoted as Cases I–IV in Table 3, are experimentally tested using the proposed HB-EMD in this study. Case I synthesizes a resistor and a capacitor connected in series, which mimics a mechanical inerter damper (ID); Case II synthesizes a resistor and an inductor connected in series, which mimics a mechanical viscoelastic damper (VED); and Cases III and IV synthesize pure resistors, which mimics VFD. The impedance parameter selections in four cases are intended to emulate mechanical behaviors of different types of mechanical dampers and meanwhile to satisfy the energy harvesting condition in Eq. (19) (i.e., $R > R_t$). These impedance parameters can be flexibly adjusted in practical applications to achieve the desirable mechanical parameters (damping, stiffness and inertance) with the constraints of Eq. (7).

The time histories of the measured current and voltage signals corresponding to the four cases are presented in Fig. 9(a)–(d), respectively. The blue lines stand for motor *emf*, the red lines denote the currents, and the green shaded areas (i.e., envelop current) represent the potential energy harvesting regions suggested by Eq. (14), whose boundaries are defined as the *emf* divided by the circuit resistance R_t. This green shaded area also corresponds to the green shaded areas in Fig. 6. In Fig. 9, the theoretical results are presented in dashed lines, whereas the measured experimental results are marked in solid lines. The good agreement between the theoretical and the experimental results suggests the successful functionality of the proposed HB-EMD system.

Table 3. Experimental cases for synthetic impedance

Case number	R (Ω)	Damping coeff. (Ns/m)	L (H)	Stiffness (N/m)	C (F)	Inertance (kg)	Freq. (Hz)
Case I	30	56	0	–	5×10^{-4}	0.84	8
Case II	30	56	1.2	1400	∞	–	8
Case III	30	56	0	–	∞	–	8
Case IV	50	34	0	–	∞	–	8

Fig. 9(a) shows the results of Case I, in which the capacitance results in the time-lead current that emulates mechanical inertance. By contrast, the time-lag effect can be observed in Fig. 9(b) (Case II), reflecting the inductance effect that is equivalent to the mechanical stiffness. In Cases I and II, the current signals periodically "enter" and "exit" the green shaded area, suggesting that the HB-EMD harvests and consumes energy in an alternate manner. By contrast, Fig. 9(c) and (d) (Cases III and IV) present pure damping effects, where the voltages and currents are always in phase with each other, and the motor currents (i) always stay within the green shaded ranges, representing a continuous energy harvesting effect. Given that the emulated resistance

values in Cases III and IV (i.e., 56 and 34 Ω, respectively) are larger than the circuit inherent resistance value (R_t = 16 Ω), as required by Eq. (19), such observations match the theoretical analysis. Note all mentioned four cases were realized using the same HB-EMD device with the only modification made to the coding introduced in Section 2.3.

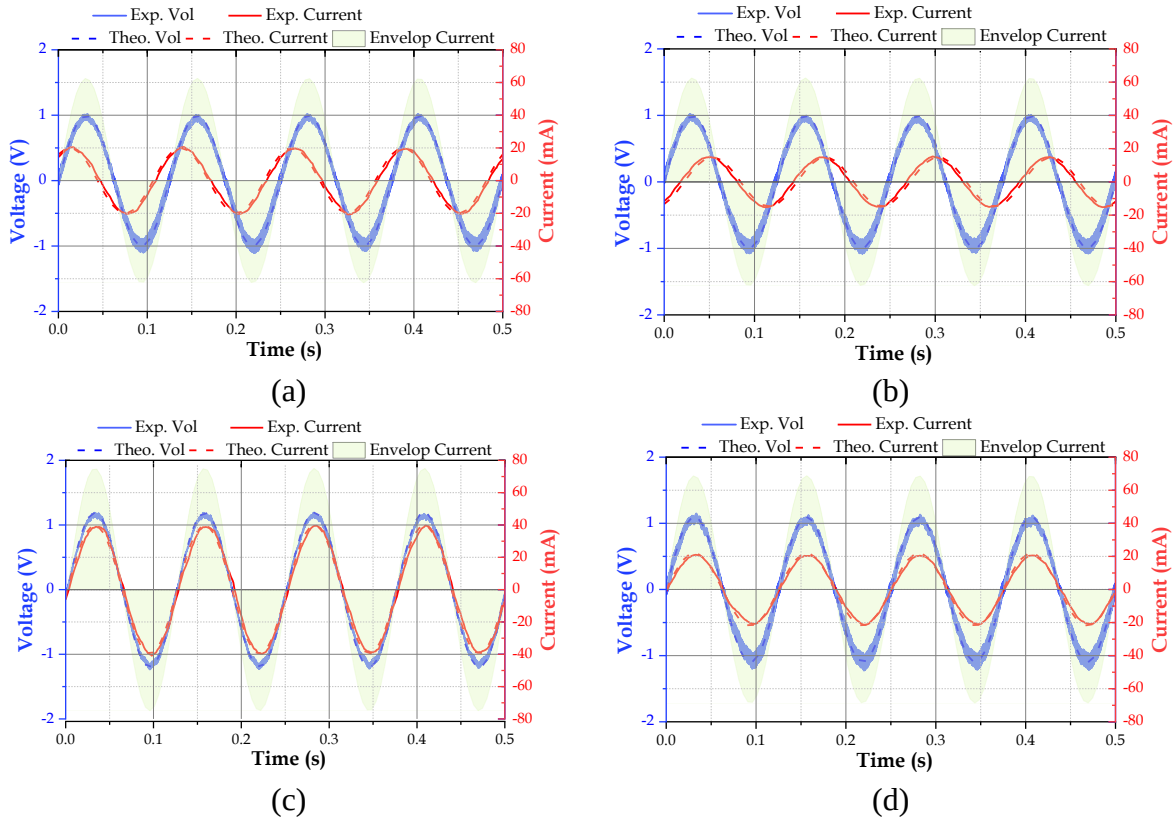

Fig. 9 Realization of the diverse behavior by HB-EMD (voltage and current in time domain): (a) Case I; (b) Case II; (c) Case III; (d) Case IV

Fig. 10(a) and (b) present the force–velocity and force–displacement diagrams, respectively, where the versatile mechanical behavior of HB-EMD can be directly perceived. The green shaded areas in Fig. 10(a) represent the energy harvesting regions that are also illustrated in Fig. 3. In Fig. 10(a), for Cases III and IV that synthesize pure resistance scenarios, nearly all areas lie within the green-colored region in the first and third quadrants; whereas for Cases I and II, the elliptic loops cover all four quadrants. Nevertheless, the areas within the green-colored regions are larger, indicting an overall energy harvesting performance. According to Eq. (19), any synthetic impedance with a real part larger than R_t (equal to 16 Ω in the experiment) should correspond to an overall energy harvesting feature. Notably, the force and velocity are in phase in Cases III and IV, and thus their relationships are nearly straight lines in Fig. 10(a); while the velocity lags behind and leads the force in Case I and Case II, respectively, which correspond to ellipses rotating in the clockwise and counterclockwise direction in Fig. 10(a), respectively.

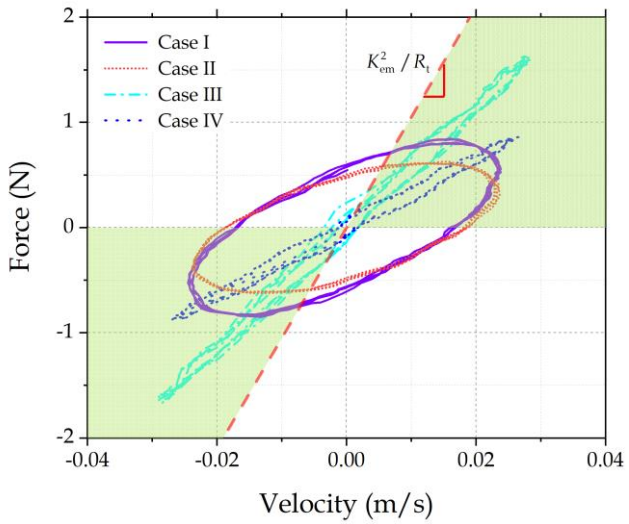

(a)

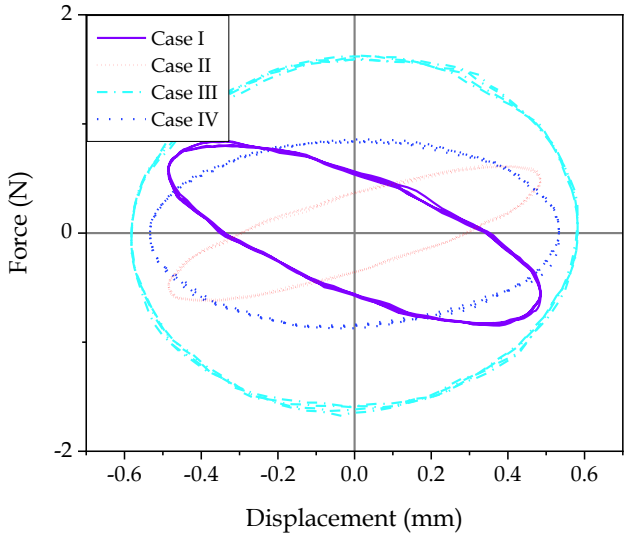

(b)

Fig. 10 Versatile behavior of HB-EMD: (a) force–velocity diagram (b) force–displacement diagram

Considering that the battery current alters its direction (charge and discharge) at a high frequency, the average power of every 4 PWM cycles is subsequently calculated. Fig. 11 further provides the time histories of the batter power for Cases I and IV, along with the motor voltage and current curves. In Fig. 11(a) (i.e., Case I), both energy harvesting and consuming processes are experienced. The vertical purple dash-dot lines mark the intersection points between the motor current and the green-colored envelope, indicating the boundaries between the mentioned two modes. This current diagram matches well with the power diagram on the second row, where the vertical purple dash-dot lines correspond to nearly zero power consumption. If the current lies within the green-colored region, then the related output power will be positive, and the battery is charged. Otherwise, the output power will be negative when the current leaves the green region, suggesting an energy consumption (actuation) process. According to Eq. (18), the theoretical average output power in Case I is 2.7 mW; whereas the

experimental results provide a value of 3.5 mW. Both results indicate an overall energy harvesting effect.

Fig. 11(b) presents the diagrams for Case IV in the emulation of pure resistance ($R > R_t$). The entire process is in an energy harvesting mode when providing a damping-like control force. On the basis of Eq. (18), the theoretical average power can be calculated as 8.3 mW, whereas the experimental reading is 7.2 mW.

It is noteworthy that this paper aims to realize the advanced self-powered HB-EMD with synthetic impedance, instead of the maximization of the output power. The HB-EMD may operate in energy harvesting and consuming modes alternately. Consequently, the harvested energy in the former mode is partially reused in the latter mode. Therefore, to achieve energy balance (i.e., slightly positive output power) is the major objective of this paper. For the applications with the major interest in energy harvesting, the control strategy of the HB-EMD should be redesigned to maximize the harvested power, e.g., eliminate the energy consuming mode in the control process.

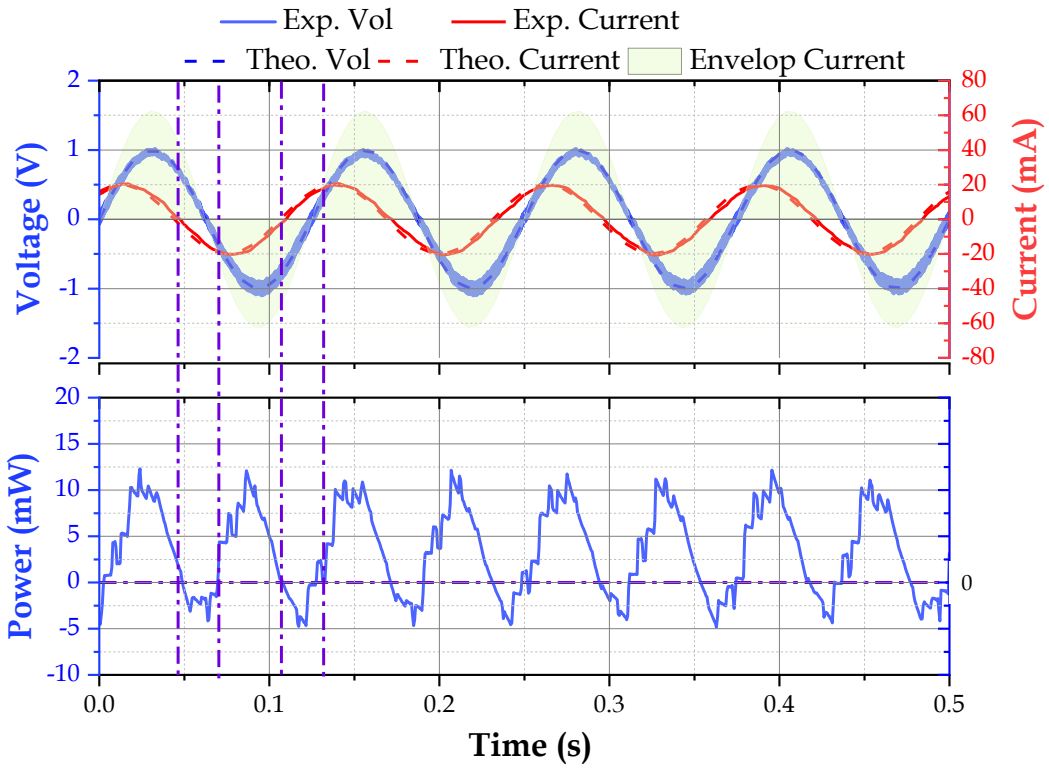

(a)

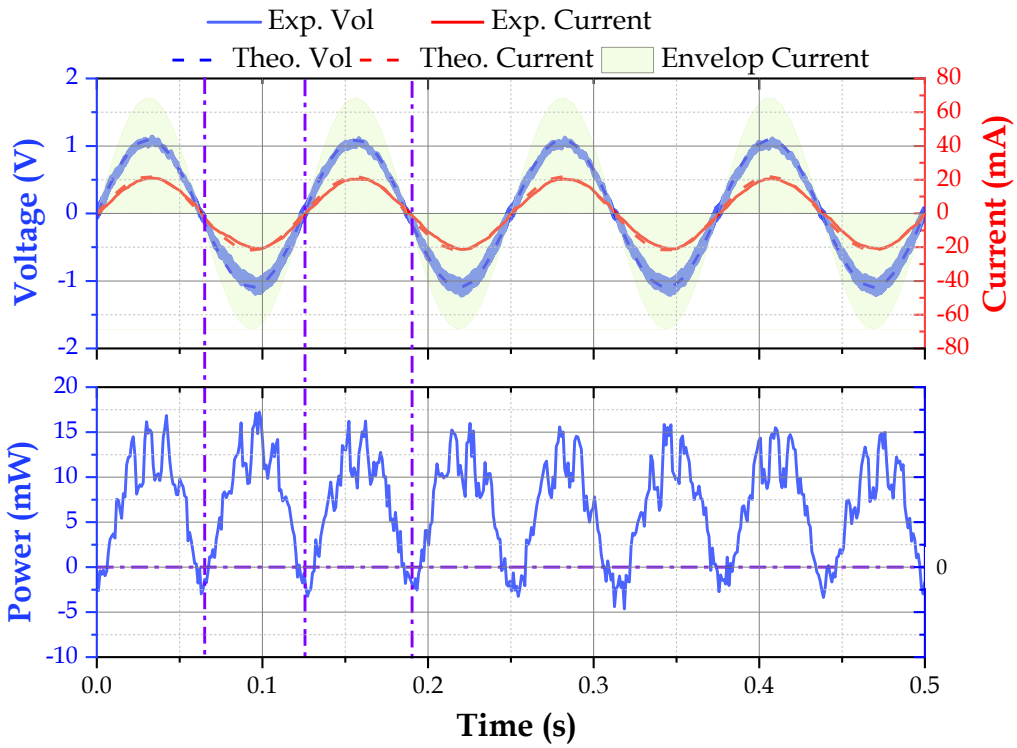

(b)

Fig. 11 Power analyses in time domain: (a) for Case I, (b) for Case IV

4. Discussion on Scalability of HB-EMD

Only a small-scale HB-EMD prototype with a relatively small damper force was tested in this study to examine the feasibility of the proposed tunable EMD concept. Large-scale HB-EMDs suitable for heavy-duty applications (e.g., the vibration control for full-scale mechanical or civil structures) need to be further investigated in the future. Some potential technical issues regarding the scalability of the proposed HB-EMD are discussed in this section.

A major concern in enlarging HB-EMD is the potential high power, including high voltages (up to hundreds of voltages) and high current (tens of amperes). Shen et al. [5] investigated an energy regenerative TMD implemented in a 76-story wind-excited benchmark building model, and the output power of the EMD ranges between 0.1 kW and 10 kW under a mean wind speed of 8–25 m/s. This output power corresponds to a current ranging between 0.5 A and 46 A, given the assumed nominal rechargeable battery voltage at V_{batt} = 216 V. Consequently, the compatibilities of four critical electrical modules in HB-EMD are examined, namely, the EM transducer, H-bridge circuit, rechargeable battery set, and MCU.

EM Transducer: High-power rotary electromagnetic transducers or generators are widely available. For instance, modified wind turbine generators accompanied by fan cooling systems can well serve the purpose. Nevertheless, such electromagnetic transducers are generally multiphase devices, which will require subsequent updates to the circuit design (e.g., the 3-phase H-bridge design).

H-Bridge: High-power MOSFET compatible to high battery voltage and currents should be used. For instance, one market available type – IXTH11025T (I_{max} = 110 A, R_{MOS} < 24 mΩ, V_{DS} = 250 V, V_{GS} = 20 V) – may serve the purpose, where I_{max} is the maximum allowable current, R_{MOS} is the inner resistance of the MOSFET, V_{DS} is the drain-source voltage, and V_{GS} is the gate-source voltage (i.e., trigger voltage). These nominal parameters cover the predicted voltage and current ranges along with allowance for marginal fluctuations.

Insulated-gate bipolar transistor (IGBT) may serve as a reasonable alternative to high-power MOSFET, when an extremely high voltage is expected (e.g., potential voltage spike). Although the operational switching frequency of IGBT (typically over 1 kHz) is generally lower than MOSFET, it remains several orders higher than the natural frequency of the target structures (i.e.., generally below 10 Hz and even below 1 Hz for certain applications, such as wind turbine and tall-buildings), thus guaranteeing the normal function of HB-EMD. For instance, HGTG18N120BND can operate up to 54 A and 1200 V.

A compatible gate driver can be IR2153 (maximum floating voltage = 625 V, clamp voltage 15.6 V), which is a common gate driver in electric vehicle applications.

Battery: Durable rechargeable batteries compatible to large voltages and high-frequency charge-cycles are expected in this application. Inspired by the mature battery technologies in electric vehicle industry, a similar battery package is considered suitable for large-scale HB-EMD. For instance, the battery package of 100 kWh (360 MJ) consisting of 7,104 cylindrical rechargeable cells (type 18,650) provides a nominal voltage of 356.4V in Tesla Model S 100D

[30]. The output voltage, energy capacity, and battery inner resistance can be flexibly adjusted to fit the scaled HB-EMD by properly rearranging the battery cells (i.e., add/remove batteries, series/parallel battery connection).

MCU: MCU in the proposed system does not directly experience high voltage or large current as seen in MOSFETs or the gate driver. Instead, the MCU mainly receives input feedback signals (e.g., velocity, acceleration, voltage, and current signals), processes the data, and outputs the corresponding control signals accordingly. Although the input signal may contain high voltages due to excessive vibration, such voltages can be reduced to a proper range by using voltage dividers. In theory, high-power applications will not affect the selection of MCU. Besides, the power consumption of MCU in large-scale applications can generally be ignored, given the typical power consumption of hundreds of milliwatts. In this regard, MCU may be upgraded to ones with high clock frequencies and enhanced computation abilities, given that its power consumption is no longer a major concern. A programmable logic controller can replace the MCU, if reliability and flexibility are particularly stressed in industrial-standard applications.

5. Conclusions

A novel HB-EMD that simultaneously enables tunable mechanical behavior via synthetic impedance and energy harvesting functions is analytically and experimentally introduced and analyzed in this paper. In particular, the system topology, working mechanism, power analyses, and realization of synthetic impedance are presented in detail. Several compatibility issues of HB-EMD to large-scale structures are also discussed. Some key conclusions of this paper are summarized as follows:

1. The proposed HB-EMD can emulate versatile behavior of different conventional mechanical dampers (such as VFD, VED, and ID) with potential energy harvesting ability. By contrast, the previous dual-function dampers can provide only pure damping behavior.

2. The behavior manipulation in HB-EMD is digitally realized by altering the coding in MCU. The synthetic impedance technique can minimize the inherent resistance of the whole circuit by avoiding the use of real electrical elements (e.g., resistors and inductors used in [3]), which will considerably benefit the energy harvesting functions. In addition, the digital adjustment of the device grants flexible tuning of the HB-EMD.

3. The emulation of various mechanical dampers by using HB-EMD in this study employs only the sensing of local motions (i.e., velocity) in the feedforward control. Nevertheless, given the available sensing, feedback, and feedforward functions, the proposed HB-EMD can be readily extended to provide advanced control (either semi-active or active) by merely updating the control algorithm and sensory systems.

4. A simple and design-friendly energy harvesting condition (i.e., $\Re(Z) > R_t$) exists in the realization of synthetic impedance.

5. The feasibility of the HB-EMD is validated through experiments, in which a total of four representative cases covering different damping, stiffness, and inertance features are included. The satisfactory agreement between the theoretical and experimental results ratifies the soundness of the system.

6. The discussion on scalability suggests that the HB-EMD can be potentially enlarged to ones compatible to large-scale mechanical or civil structures. The prospects of large-scale industrial-standard HB-EMD needs to be systematically investigated in the future.

Acknowledgment

The authors are grateful for the financial support from the Research Grants Council of Hong Kong (Nos.: PolyU 15214620, N PolyU533/17, PolyU R5020-18, and T22-502/18-R). The first author also gratefully acknowledges the support from the Postdoc Matching Fund Scheme from The Hong Kong Polytechnic University (PP0034914). The findings and opinions expressed in this paper are from the authors alone and are not necessarily the views of the sponsors.

References

[1] G. W. Housner *et al.*, "Structural Control: Past, Present, and Future," *Journal of Engineering Mechanics*, vol. 123, no. 9, pp. 897-971, 1997, doi: 10.1061/(asce)0733-9399(1997)123:9(897).

[2] T. T. Soong, "State-of-the-art review: Active structural control in civil engineering," *Engineering Structures*, vol. 10, no. 2, pp. 74-84, 1988, doi: 10.1016/0141-0296(88)90033-8.

[3] J.-Y. Li and S. Zhu, "Versatile Behaviors of Electromagnetic Shunt Damper With a Negative Impedance Converter," *IEEE/ASME Transactions on Mechatronics*, vol. 23, no. 3, pp. 1415-1424, 2018, doi: 10.1109/tmech.2018.2813307.

[4] R. Palomera-Arias, J. J. Connor, and J. A. Ochsendorf, "Feasibility Study of Passive Electromagnetic Damping Systems," *Journal of Structural Engineering*, vol. 134, no. 1, pp. 164-170, 2008, doi: 10.1061/(asce)0733-9445(2008)134:1(164).

[5] W. Shen, S. Zhu, Y.-L. Xu, and H.-P. Zhu, "Energy regenerative tuned mass dampers in high-rise buildings," *Structural Control and Health Monitoring*, vol. 25, no. 2, pp. 1-18, 2018, doi: 10.1002/stc.2072.

[6] X. Tang and L. Zuo, "Simultaneous energy harvesting and vibration control of structures with tuned mass dampers," *Journal of Intelligent Material Systems and Structures*, vol. 23, no. 18, pp. 2117-2127, 2012, doi: 10.1177/1045389x12462644.

[7] L. Zuo and X. Tang, "Large-scale vibration energy harvesting," *Journal of Intelligent Material Systems and Structures*, vol. 24, no. 11, pp. 1405-1430, 2013, doi: 10.1177/1045389x13486707.

[8] W. Shen, "Electromagnetic damping and energy harvesting devices in civil structures," The Hong Kong Polytechnic University, 2014.

[9] N. Makris, "Viscous heating of fluid dampers. I: Small-amplitude motions," *Journal of engineering mechanics*, vol. 124, no. 11, pp. 1210-1216, 1998.

[10] B. Yan, K. Wang, Z. Hu, C. Wu, and X. Zhang, "Shunt Damping Vibration Control Technology: A Review," *Applied Sciences*, vol. 7, no. 5, 2017, doi: 10.3390/app7050494.

[11] S. Behrens, A. J. Fleming, and S. O. R. Moheimani, "Electromagnetic shunt damping," 2003 2003, vol. 2: IEEE, pp. 1145-1150.

[12] S. Behrens, A. J. Fleming, and S. O. R. Moheimani, "Passive Vibration Control via Electromagnetic Shunt Damping," (in en), *IEEE/ASME Transactions on Mechatronics,* vol. 10, no. 1, pp. 118-122, 2005/02// 2005, doi: 10.1109/TMECH.2004.835341.

[13] T. Inoue, Y. Ishida, and M. Sumi, "Vibration Suppression Using Electromagnetic Resonant Shunt Damper," *J. Vib. Acoust.,* vol. 130, no. 4, pp. 1-8, 2008/07/01 2008, doi: 10.1115/1.2889916.

[14] H. Zhu, Y. Li, W. Shen, and S. Zhu, "Mechanical and energy-harvesting model for electromagnetic inertial mass dampers," *Mechanical Systems and Signal Processing,* vol. 120, pp. 203-220, 2019, doi: 10.1016/j.ymssp.2018.10.023.

[15] D. Ning *et al.*, "An electromagnetic variable inertance device for seat suspension vibration control," *Mechanical Systems and Signal Processing,* vol. 133, 2019, doi: 10.1016/j.ymssp.2019.106259.

[16] B. Yan, H. Ma, L. Zhang, W. Zheng, K. Wang, and C. Wu, "A bistable vibration isolator with nonlinear electromagnetic shunt damping," *Mechanical Systems and Signal Processing,* vol. 136, pp. 1-19, 2020, doi: 10.1016/j.ymssp.2019.106504.

[17] S. Li, J. Xu, X. Pu, T. Tao, and X. Mei, "A novel design of a damping failure free energy-harvesting shock absorber system," *Mechanical Systems and Signal Processing,* vol. 132, pp. 640-653, 2019-10-01 2019, doi: 10.1016/j.ymssp.2019.07.004.

[18] R. Zhang and X. Wang, "Parameter study and optimization of a half-vehicle suspension system model integrated with an arm-teeth regenerative shock absorber using Taguchi method," *Mechanical Systems and Signal Processing,* vol. 126, pp. 65-81, 2019-07-01 2019, doi: 10.1016/j.ymssp.2019.02.020.

[19] A. Gonzalez-Buelga, L. R. Clare, S. A. Neild, J. Z. Jiang, and D. J. Inman, "An electromagnetic inerter-based vibration suppression device," *Smart Mater. Struct.,* vol. 24, no. 5, p. 055015, 2015/05/01/ 2015, doi: 10.1088/0964-1726/24/5/055015.

[20] S. Zhu, W. Shen, and X. Qian, "Dynamic analogy between an electromagnetic shunt damper and a tuned mass damper," (in en), *Smart Mater. Struct.,* vol. 22, no. 11, pp. 1-11, 2013 2013, doi: 10.1088/0964-1726/22/11/115018.

[21] S. Zhu, W. Shen, and Y. Xu, "Linear electromagnetic devices for vibration damping and energy harvesting: Modeling and testing," *Engineering Structures,* vol. 34, pp. 198-212, 2012/01// 2012, doi: 10.1016/j.engstruct.2011.09.024.

[22] W. Shen, S. Zhu, and Y.-l. Xu, "An experimental study on self-powered vibration control and monitoring system using electromagnetic TMD and wireless sensors," *Sensors and Actuators A: Physical,* vol. 180, pp. 166-176, 2012/06// 2012, doi: 10.1016/j.sna.2012.04.011.

[23] C.-Y. Hsieh, M. Moallem, and F. Golnaraghi, "A Bidirectional Boost Converter With Application to a Regenerative Suspension System," *IEEE Transactions on Vehicular Technology,* vol. 65, no. 6, pp. 4301-4311, 2016, doi: 10.1109/tvt.2015.2504458.

[24] C.-Y. Hsieh, B. Huang, F. Golnaraghi, and M. Moallem, "Regenerative Skyhook Control for an Electromechanical Suspension System Using a Switch-Mode Rectifier," *IEEE Transactions on Vehicular Technology,* vol. 65, no. 12, pp. 9642-9650, 2016, doi: 10.1109/tvt.2016.2524693.

[25] J. A. Bowden, S. G. Burrow, A. Cammarano, L. R. Clare, and P. D. Mitcheson, "Switched-Mode Load Impedance Synthesis to Parametrically Tune Electromagnetic Vibration Energy Harvesters," *IEEE/ASME Transactions on Mechatronics,* vol. 20, no. 2, pp. 603-610, 2015, doi: 10.1109/tmech.2014.2325825.

[26] P. D. Mitcheson, T. T. Toh, K. H. Wong, S. G. Burrow, and A. S. Holmes, "Tuning the Resonant Frequency and Damping of an Electromagnetic Energy Harvester Using Power Electronics," *IEEE Transactions on Circuits and Systems II: Express Briefs,* vol. 58, no. 12, pp. 792-796, 2011, doi: 10.1109/tcsii.2011.2173966.

[27] Y. Liu, G. Tian, Y. Wang, J. Lin, Q. Zhang, and H. F. Hofmann, "Active Piezoelectric Energy Harvesting: General Principle and Experimental Demonstration," *Journal of Intelligent Material Systems and Structures,* vol. 20, no. 5, pp. 575-585, 2009, doi: 10.1177/1045389x08098195.

[28] A. J. Fleming, S. Behrens, and S. O. R. Moheimani, "Synthetic impedance for implementation of piezoelectric shunt-damping circuits," *Electronics Letters*, vol. 36, no. 18, 2000, doi: 10.1049/el:20001083.

[29] J. Necasek, J. Vaclavik, and P. Marton, "Digital synthetic impedance for application in vibration damping," *Rev Sci Instrum*, vol. 87, no. 2, p. 024704, Feb 2016, doi: 10.1063/1.4942085.

[30] M. Pressman. "Understanding Tesla's lithium ion batteries." https://evannex.com/blogs/news/understanding-teslas-lithium-ion-batteries#:~:text=The%20most%20popular%20battery%20pack,to%2090%20kWh%20of%20energy. (accessed.